Turbulence Power Spectra in Regions Surrounding Jupiter's South Polar Cyclones from Juno/JIRAM

M.L.Moriconi[1], A. Migliorini[2], F. Altieri[2], A. Adriani[2], A. Mura[2], G. Orton[3], J. I. Lunine[4], D. Grassi[2], S. K. Atreya[5], A. P. Ingersoll[6], B. M. Dinelli[1], S. J. Bolton[7], S. Levin[3], F. Tosi[2], R. Noschese[2], C. Plainaki[8], A. Cicchetti[2], G. Sindoni[8] and A. Olivieri[8].

[1]CNR-Istituto di Scienze dell'Atmosfera e del Clima, Bologna, Italy
[2]INAF-Istituto di Astrofisica e Planetologia Spaziali, Rome, Italy
[3]Jet Propulsion Laboratory, California Institute of Technology, 4800 Oak Grove Drive Pasadena, CA 91109 USA
[4]Cornell University, 410, Thurston Avenue, NY 14850-2488 USA
[5]University of Michigan, Climate and Space Sciences and Engineering Department, Ann Arbor, MI 48109 USA
[6]California Institute of Technology, 1200 E. California Blvd., Pasadena, CA 91125 USA
[7]Southwest Research Institute, 6220 Culebra Road, San Antonio, TX 78238 USA
[8]Agenzia Spaziale Italiana, Via del Politecnico snc, 00133 Roma, Italy

Key Points:

- Dynamics consistent with quasi-geostrophic 2D turbulence in the Jupiter South Polar regions surrounding the main cyclonic circulations.
- The forcing scales resulting from these analyses indicate that baroclinic instabilities may exist in the analyzed regions.
- Many waves have been revealed in the Jupiter South Polar region by JIRAM images.

Abstract

We present a power spectral analysis of two narrow annular regions near Jupiter's South Pole derived from data acquired by the Jovian Infrared Auroral Mapper (JIRAM) instrument onboard NASA's Juno mission. In particular, our analysis focuses on the dataset acquired by the JIRAM M-band imager (hereafter IMG-M) that probes Jupiter's thermal emission in a spectral window centered at 4.8 μm. We analyze the power spectral densities of circular paths outside and inside of cyclones on images acquired during six Juno perijoves (PJ). The typical spatial resolution is around 55 km pixel^{-1}. We limited our analysis to six acquisitions of the South Pole from February 2017 to May 2018. The power spectral densities both outside and inside the circumpolar ring seem to follow two different power laws. The wavenumbers follow average power laws of -0.9±0.2 (inside) and -1.2±0.2 (outside), and of -3.2±0.3 (inside) and -3.4±0.2 (outside), respectively beneath and above the transition in slope located at ~ 2.×10^{-3} km^{-1} wavenumber. This kind of spectral behavior is typical of two-dimensional turbulence. We interpret the 500 km length scale, corresponding to the transition in slope, as the Rossby deformation radius. It is compatible with the dimensions of a subset of eddy features visible in the regions analyzed, suggesting that a baroclinic instability may exist. If so, it means that the quasi-geostrophic approximation is valid in this context.

This is the author manuscript accepted for publication and has undergone full peer review but has not been through the copyediting, typesetting, pagination and proofreading process, which may lead to differences between this version and the Version of Record. Please cite this article as doi: 10.1029/2019JE006096

Plain Language Summary

Juno has revealed extraordinary and unexpected dynamics in Jupiter's polar regions. The clouds imaged in the infrared and visible parts of the spectrum by JIRAM and JunoCam, respectively, are organized around a central cyclone in regular patterns of eight (North Pole) and five (South Pole) cyclones. We studied the spatial and temporal variability of the regions immediately outside the cyclonic circulations at the South Pole. By analyzing multiple JIRAM images at 5 microns, geographically merged and appropriately filtered and sampled, we found that cloud patterns poleward and equatorward the ring of cyclones at Jupiter's South Pole, may originate from flow instabilities not linked to vortices' dynamics. These instabilities can have their origin in the horizontal pressure and temperature gradients rather than in the cyclonic circulations and their interactions, also considering the low speed values of the wind field in those regions.

Keywords: Jupiter; Planetary atmospheres; Polar regions; Turbulence; Fourier analysis

1. Introduction

The design of Juno's orbital tour permitted the detailed observation of Jupiter's hitherto unexplored polar regions. In particular, infrared and visible observations obtained by JIRAM and JunoCam instruments, respectively (Adriani et al., 2019, 2018; Orton et al., 2017), revealed an unexpected cluster of cyclones organized in a polygonal array, which has persisted between at least 2017-02 and 2018-05. The dynamics at the root of this configuration, which is unique in the Solar System, are not yet completely understood, though certain recent studies provide some hint of the possible underlying mechanisms (Reinaud, 2019; Brueshaber et al., 2019). Power spectral analysis previously has been used to study aspects of the dynamical mechanisms operating at various scales on cloud patterns of various planetary atmospheres (Travis, 1978; Harrington et al., 1996; Peralta et al., 2007; Barrado-Izagirre et al., 2009; Choi & Showman, 2011; Cosentino et al., 2017, Young & Read, 2017, Cosentino et al., 2019). Power spectral density is a practical way to capture the statistics of cloud fields over several wavenumber scales and can quantify the type of turbulence acting in the atmosphere by describing the distribution of energy at various scales across the Fourier components. The study of atmospheric kinetic energy transfer, implicit in the power spectrum, generally requires the wind field measurement to have an accuracy better than 5 m/sec (Sada et al., 1996; Travis,1978), a goal that is very difficult to achieve over large areas by the instruments onboard current space missions. However, the connection between power spectra of cloud opacities/albedo and those of atmospheric kinetic energy, empirically established by Travis (1978), has been assumed in many previous studies (Harrington et al., 1996; Peralta et al., 2007; Barrado-Izagirre et al., 2009; Choi & Showman, 2011; Cosentino et al., 2017, Young & Read, 2017, Cosentino et al., 2019).

A puzzling question raised by the unexpected dynamical configuration of Jupiter's poles is whether the cluster of polar vortices observed by JIRAM and JunoCam is tied to a deep magneto-hydrodynamic circulation, or instead is a more or less stable configuration in the weather layer

supported by energy forcing from moist convection or other energy transport mechanisms (Sánchez-Lavega & Heimpel, 2018). Both the deep-convection and shallow-water models, with hybrid combinations, have been developed as general circulation hypotheses in past years (Sánchez-Lavega & Heimpel, 2018, and references therein), aiming initially to reproduce Jupiter's banded aspect and velocities of its jets. None of these models simulated the possible dynamical structure of the polar regions. We believe that it is premature to confidently assert which of these models works better to explain the Jupiter's poles, as observed by Juno/JIRAM. Our goal in this work is to investigate what kind of dynamics prevails in those polar regions out of the main cyclonic circulations. While one of the full polar cyclones is analyzed in the paper of Adriani et al. (2019) by using 2D Fourier analysis, here we use 1D Fourier spectral analysis to investigate whether the dynamics in areas surrounding the main cyclones are compatible with quasi-geostrophic two-dimensional turbulence. We aim also to determine whether any changes in eddy statistics occurred between the several-month-long intervals when JIRAM observed the whole polar region. Two-dimensional turbulence is typical of large-scale motions of geophysical fluids in a shallow-water scenario (Danilov & Gurarie, 2000), and this model has been already successfully tested in the case of Jupiter's middle and low latitudes in past years (Harrington et al., 1996; Barrado-Izagirre et al., 2009; Choi & Showman, 2011; Cosentino et al., 2017, Young & Read, 2017, Cosentino et al., 2019). In our case, we have large horizontal coverage associated with a depth of sounding as yet unknown and dependent on the vertical extent and optical depth of the cloud layers that constitute the pattern imaged by JIRAM.

For a clear atmosphere, the whole thickness of JIRAM penetration (~150 km) related to the circumference relative to 87°S planetographic latitude (~25000 km) would give a scale $O(10^2)$, thus a larger emphasis of the horizontal respect to the vertical scale. However, from a dynamical point of view, whether a phenomenon is to be considered a large-scale one depends on how much it is influenced by the planet's rotation, as well as on its size. Therefore, the choice of the brightness scans, from which we extract signal samples to analyze, is a complicated matter. The cluster of cyclones (Adriani et al., 2018) could well have its origin deeper than the weather layer, in the light of current knowledge, while the regions outside and inside the circumpolar ring of cyclones are probably confined at some level in the weather layer. For this reason, we oriented our study to signals sampled in those regions. This has been accomplished by tracing some *ad hoc* circular paths, outside and inside the cyclonic ring (Figure 1), from which we extracted radiance signal samples. Henceforth we will refer to these two annular regions also as "equatorward" and "poleward" respectively, with respect to the ring of cyclones. Because small vortices are ubiquitous in the regions under study and they can influence the power spectral slopes (Barrado-Izagirre et al., 2009), paths have been traced in areas as uniform as possible, as explained in detail in section 2, minimizing the presence of the small vortices.

This work is organized into six sections. In section 2 we provide information on the instrument and describe the observations and the processing applied in order to obtain the mosaic of the entire polar region. We outline also the criteria used to select the sample data to analyze. In section 3, we give details of the analysis we carried out and in section 4 we search for wave presence in the analyzed region. The principal findings are discussed in section 5 in terms of models and previous turbulence results. A summary of our conclusions is reported in section 6.

2. Data and methodology

JIRAM combines an infrared imager and a slit spectrometer, sharing the same telescope. The imager focal plane is in turn divided into two equal areas defined by the superimposition of two different band-pass filters: the L-filter, centered at 3.45 μm with a 290 nm bandwidth (IMG-L), and the M-filter, centered at 4.78 μm with a 480 nm bandwidth (IMG-M). The spectrometer covers the spectral region from 2 to 5 μm (average spectral sampling 9 nm/band) with a 256 pixels slit, co-located in the M-filter imager's Field of View (FOV) (Adriani et al., 2014).

Juno's highly elliptical ~53 day polar orbit around Jupiter makes it possible to acquire very close snapshots of the polar regions by JunoCam and JIRAM. During the spacecraft passages over Jupiter's poles, the instruments have the opportunity to sense adjacent regions of the underlying cloud deck. In some passages JIRAM had the opportunity to cover almost completely the polar regions. IMG-M acquired data sessions at approximately 10-minutes time steps, wherein every session is a collection of observations acquired every ~ 30 s. In this work, we use the images of the South Pole acquired during the fourth, sixth, eighth, ninth, eleventh and thirteenth orbits (PJ4, PJ6, PJ8, PJ9, PJ11 and PJ13 passages), spanning an overall period of roughly 1.5 years. These datasets provide full coverage from the 82.5° S planetographic latitude poleward, except the PJ9 and PJ13 cases, where a small area is missing. Unfortunately, the spacecraft attitude did not permit the complete coverage of the northern regions during the same orbits and the North Pole had only a partial coverage, except for the PJ4 passage. Therefore, we prefer to limit our investigation to the South Pole. A list of IMG-M image sequences used in this study along with the proper pixel resolution (km) and time coverage for each sequence is reported in Supplemental Material 1.

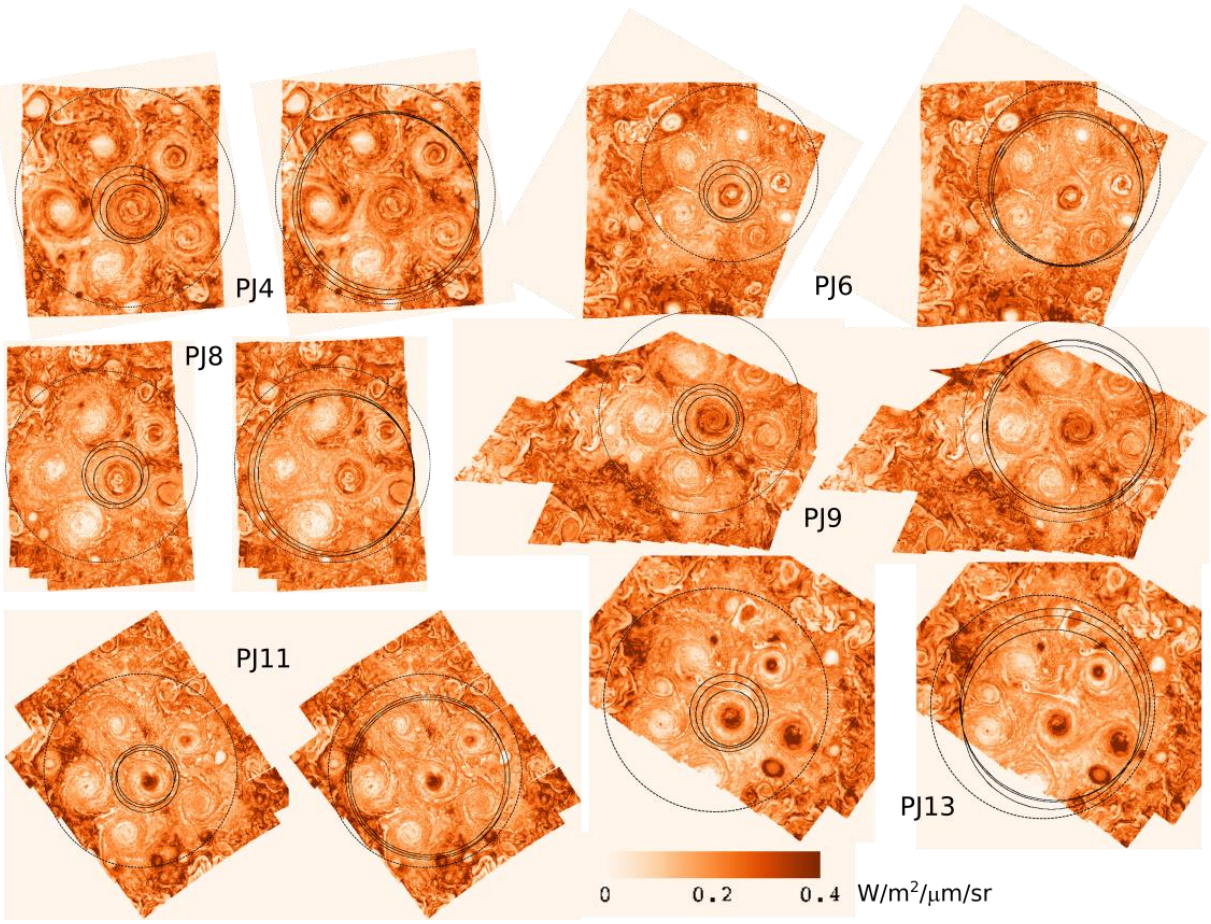

Figure 1- Stereographic projections of mosaics composed with images of Jupiter's South Pole acquired by IMG-M in six Juno perijoves. All the images have been corrected for the emission angle and re-scaled in the same range of radiance values. Here, aerosol-free regions of high radiance are dark, and aerosol-covered regions of low radiance are white, as reported in the color bar at the bottom of the figure. Black solid circles indicate the trajectories along which the analyzed signals have been sampled. The 80° S planetographic latitude is reported as reference (black dotted circle) in each mosaic.

In principle, JIRAM can sound atmospheric pressure levels as large as 5 bar (Kunde et al., 1982; Irwin et al.,2001, Grassi et al., 2017) in absence of thick opaque clouds, whereas in areas where thick cloud cover blocks the thermal emission from the deeper warmer interior JIRAM senses the cooler temperatures of the cloud top. All the single images by IMG-M, used to create the mosaics, have been corrected for the emission angle (that is the angle formed by the instrument line of sight and the nadir direction) and then re-projected in stereographic maps to the worst pixel resolution, that is the instantaneous FOV (IFOV) of the farthest observation of IMG-M (~ 55 km pixel^{-1}). Projected images are shown in Figure 1. We generated six mosaics for the South Pole on geographical basis, by using geometric information derived through SPICE-based routines (http://naif.jpl.nasa.gov) and navigational databases (Acton, 1996), and ENVI tools (https://www.harrisgeospatial.com/Software-Technology) for each of the geometric calibrations and image processing applied to the JIRAM images. All the maps are based on Jupiter's planetographic latitude and System III longitudes, but with longitude increasing eastward (0-360). All the images used to create the mosaics (see Table T1 as supporting information) have been acquired in a time interval where, at the mean flow estimated velocity (Grassi et al., 2018), any

possible cloud displacement is below the pixel resolution. The data range of the six South Pole mosaics has been adjusted to be in the same interval of radiance values and a color scale has been used to highlight the different optical depths, with the lowest radiance value in white and the highest one in orange (Figure 1). Hence, we show white cold clouds on an orange hot background.

We use power spectra to characterize the statistics of cloud opacities outside and inside the circumpolar ring of cyclones. These two regions have similarities from a dynamical viewpoint: both of them are marked by low wind speeds but nevertheless various morphological structures seem to suggest they are "active". The equatorward region is characterized by the interaction of the circumpolar vortices with chaotic eddy patterns outside the ring and by the mutual interplay of the vortices themselves. Similarly, the poleward region is the interaction field between the central and circumpolar cyclonic circulations. Although very low flow velocities seem to characterize these areas (at the limit of 12 m/s, the minimum detectable wind speed according to Grassi et al., 2018), they do not give the impression of being inactive (Figure 1): streams of thinning and thickening clouds and small isolated eddies are clearly visible. Therefore, we investigated these areas using power spectral analysis to characterize the resulting cloud statistics and to verify if the behavior is consistent with a 2D turbulence, as reported in Harrington et al. (1996), Barrado-Izagirre et al. (2009), Choi & Showman (2011), Cosentino et al. (2017), Young & Read (2017), Cosentino et al., (2019) for regions at lower latitudes.

We extracted from each mosaic six circular samples (black circles in Figure 1), three outside and three inside the vortex ring, which we take to be the annular region enclosing the main cyclonic circulations. We calculated the power spectrum for every sample, then, to reduce the noise, we produced two mean power spectra for the equatorward and for the poleward triplet by averaging on each single triplet power spectrum. More details on the calculations are given in section 3. Circular paths are advantageous because they combine suitable data size with the continuity of the sample, which is periodic, assuring the stationarity of the series (Bendat & Piersol, 1986). Each circular path has been shaped on latitude circles that vary from -82.5° to -83.5° for the equatorward area, and from -87° to -88° for the poleward one. These paths then had to be moved from the original latitude grid into the areas previously selected for the analysis, because of the asymmetry of the polygon of cyclones related to the geographical pole position. Particular care has been taken to avoid overlapping with the cyclones' edges, that we identify as those regions where the average intensity of the azimuthal wind is larger than ~ 50 m sec^{-1} (Grassi et al., 2018).

Equatorward paths from PJ9 and PJ13 enclose a small region outside the mosaic. We assume for these cases that the series are still stationary, like those with continuous paths, basing this assumption on similarity considerations.

The signals so produced are spatial series of pixel radiances as a function of the cumulative distance from an arbitrary starting point (pixel 1) up to the last point before pixel 1 on the circular path.

3. Power Spectral Analysis

We compute the power spectra of Jupiter's cloud opacities at the South Pole applying the Fast Fourier Transform (FFT) method to the datasets sampled on each circular path shown in Figure 1. However, because the FFT needs evenly sampled series, we resampled our datasets at even steps, applying to every sample an algorithm performing a series of weighted-least squares fits, with Gaussian weights, operating on a spatial grid equal to the IFOV (~ 55 km pixel^{-1}) in a moving window across the data. In Figure S2 of Supplemental Material 2 the PJ9 equatorward brightness scan is reported, before and after the resampling operation, as an example. The residuals from the comparison, reported as the difference between the sample data value and the ones predicted from the fit, are also shown.

The resulting signals have been tested for stationarity (Bendat & Piersol, 1986), searching for the presence of a possible trend in the spatial series, although the choice of the circular path should ensure no trends. This test gave negative results, confirming the correctness of our assumption of stationarity. In view of the successive average operation to reduce spectral noise, the spatial series have been standardized by removing the sample mean. To reduce the side-band leakage effects we applied the Hanning tapering window (Bendat & Piersol, 1986) to every power spectrum. Then we normalized for the variances of the signals and zero-padded all the sample data to the 2^{11} constant value, to ensure uniformity in length and bin size of the wavenumber range, thus making the single power spectra suitable for averaging. Because all these operations do not modify the spectral behavior, they have no impact on the principal aim of this study. The power spectra that we obtain are functions of the wavenumber (km^{-1}) and are plotted in logarithmic scale to highlight

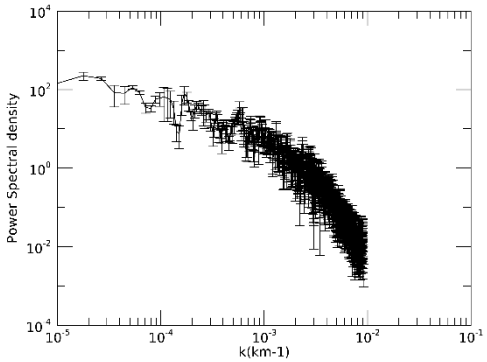

Figure 2- Average of three power spectral densities relative to the signals sampled outside the southern circumpolar ring of cyclones during PJ4. The error bars represent the standard error of the mean.

the potential presence of power-law relationships in the inertial sub-range region of the spectrum. Finally, we computed average power spectra for the regions outside and inside the circumpolar ring. In Figure 2 we show the average power spectral density (psda hereafter) of the signals

219 outside the circumpolar ring, relative to the PJ4 passage. The error bars on the spectral curve are
220 the standard error of the mean $\sigma_a = \sigma/\sqrt{N}$ (Bevington & Robinson, 1992). By a simple visual

221 inspection, the psda of Figure 2 seems to show two different slopes. To verify this hypothesis, we
222 wrote an algorithm for fitting two independent slopes, one at low and one at high wavenumbers,
223 following the approach of Choi and Showman (2011). Similar to their work, our algorithm finds

224 the best power-law relationships through linear least-squares fitting, constraining only the starting
225 and the final wavenumbers, and it determines the location of the wavenumber where the possible
226 transition in slope occurs by calculating the two independent best-fit slopes for each possible

227 transition point in the wavenumber range. The overall best fit is the one with the lowest $\chi^2 = \chi_1^2 +$

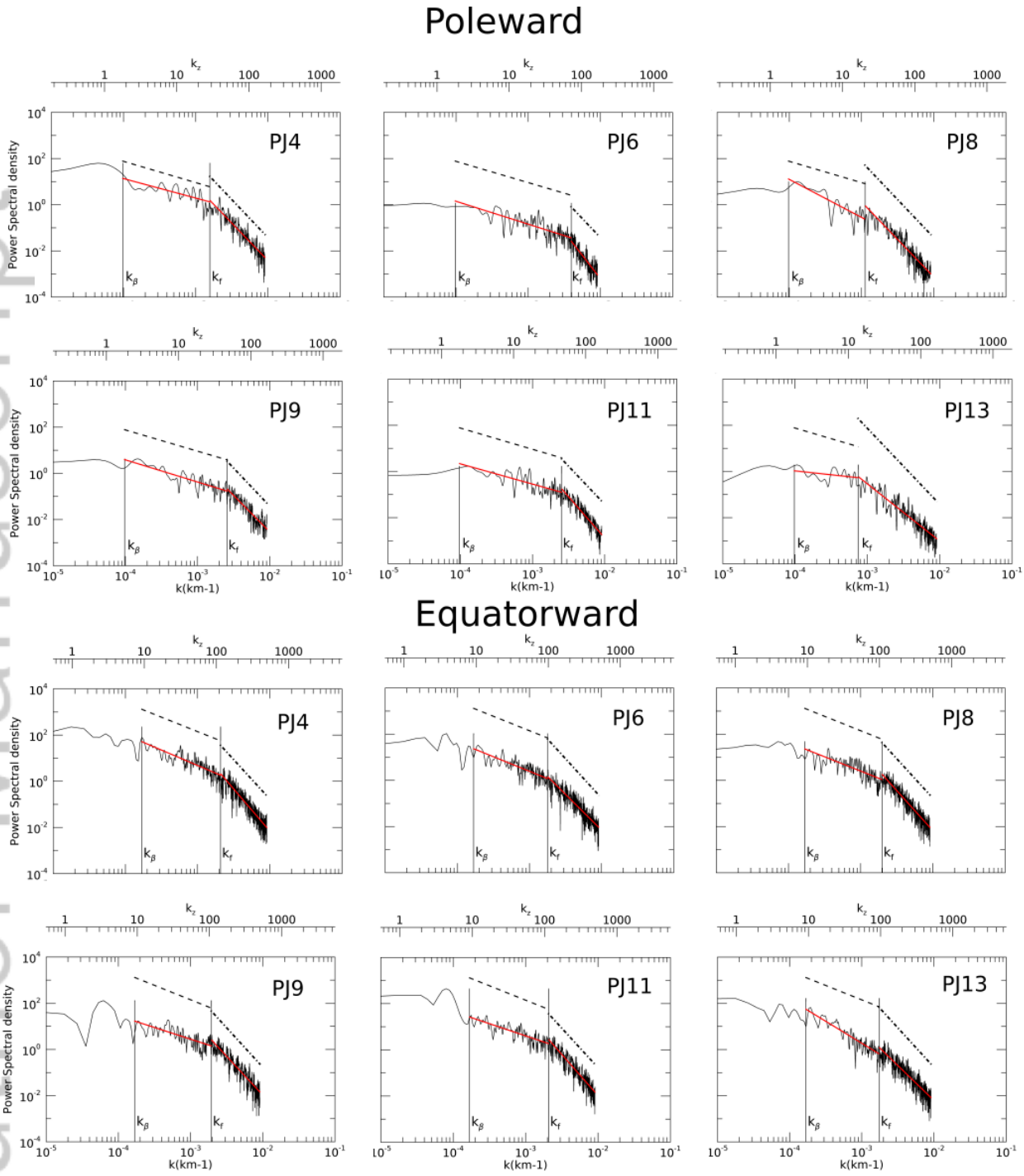

Figure 3- Averages of power spectra of the signals sampled inside (top) and outside (bottom) the southern circumpolar ring of cyclones. Power law fits overlap the spectra (red line). Median values of the overall power laws for the two cases are shown above the spectra (dashed black lines). The positions of the wavenumbers corresponding to the Rhines scale (k_β) and to the transition in slope (k_f) are marked by vertical lines. X axes at bottom of each plot are in wavenumbers – inverse of length – while x axes at the top are in zonal wavenumbers, as defined in the text.

228 χ_2^2. In Figure S3 of Supplemental Material 2 the χ^2 relative to Figure 3 plots are shown.

The maximum wavenumber of the whole best-fit range is fixed by the Nyquist theorem, but the minimum value is not so easy to constrain. In past works (Harrington et al., 1996; Barrado-Izagirre et al., 2009; Choi and Showman, 2011), different values have been assumed on the basis of the particular context, type of measurements and specific objectives of the research. In our study, we test the hypothesis that the interacting regions of the polar cyclones exhibit a dynamical state compatible with quasi-geostrophic two-dimensional turbulence, characterized by the conservation of the potential vorticity (PV) and small Rossby number (Pedlosky, 1986). This hypothesis makes straightforward the identification of the beginning of the power-law at low wavenumbers with the end of the inverse cascade inertial range. Thus, we constrain the starting value of the variation range of the overall best fit with the wavenumber value corresponding to the Rhines scale (Rhines, 1975; Ingersoll et al., 2004)

$$k_\beta = \sqrt{\frac{\beta}{2U}}$$

where U is a typical value of the horizontal wind velocity, $\beta = 2\Omega\cos(\varphi)/R$ is the local derivative

Poleward

Perijove's passes	Slope 1	Slope 2	Transition wavenumber (km^{-1})
Pj4	-0.8±0.3	-3.2±0.3	1.6e-03
Pj6	-0.8±0.2	-3.7±0.9	3.9e-03
Pj8	-1.6±0.5	-3.2±0.3	1.1e-03
Pj9	-1.0±0.3	-3.2±0.5	2.6e-03
Pj11	-0.9±0.3	-3.6±0.5	2.5e-03
Pj13	-0.3±0.7	-2.5±0.7	7.4e-04
median	-0.9±0.2	-3.2±0.3	2.0e-03±9.3e-04

Equatorward

Perijove's passes	Slope 1	Slope 2	Transition wavenumber (km^{-1})
Pj4	-1.3±0.3	-3.6±0.4	2.1e-03
Pj6	-1.3±0.4	-3.1±0.3	1.8e-03
Pj8	-1.2±0.3	-3.5±0.4	2.0e-03
Pj9	-1.0±0.3	-3.4±0.3	1.9e-03
Pj11	-1.1±0.3	-3.6±0.4	2.1e-03
Pj13	-1.9±0.3	-3.0±0.3	1.7e-04
median	-1.2±0.2	-3.4±0.2	2.0e-03±1.3e-04

Table 1-Best-fit slope values for the psda of the datasets relative to different perijoves. "Poleward" and "Equatorward" table sections correspond to psda computed by signals sampled inside and outside the circumpolar ring of cyclones. We report the values of the two slopes, the 1-σ uncertainty value for each slope fit and the wavenumber value in correspondence of the transition in slope. At the bottom of each column of the table the medians are shown.

of the Coriolis parameter with respect to the latitude φ, and Ω and R are the rotation rate and the radius of the planet. It is worthwhile mentioning that the Rhines scale may characterize many different phenomena rather than being just the scale of the cascade arrest, as stressed in the detailed study of Sukoriansky et al. (2007). However, in the absence of another objective criterion that fixes the end of the linear portion of the log-log spectral curve at low wavenumbers, the Rhines scale, intended as a sink for the energy inverse cascade (see also Cosentino et al. (2019)), is a reasonable parameter to mark the beginning of the inertial subrange. Here, two different U values (20 m s^{-1}, 15 m s^{-1}) have been assigned for equatorward and poleward regions, on the basis of the findings of Grassi et al. (2018). The values of the Rhines scale calculated from our results are in the range k ~ 1-1.5× 10^{-4}, corresponding to an interval ~ 2-8 in terms of zonal wavenumber $k_z = \frac{2\pi R(\varphi)cos(\varphi)}{1/k}$. These values are very different from the ones reported in Cosentino et al. (2019) and references therein. However, it should not be forgotten that dynamic and thermodynamic equilibria at poles can be very different from those at mid-to-low latitudes, where the values reported in literature have been computed. A physical interpretation of the sizes of the structures corresponding to the limit of the inverse cascade energy is beyond the scope of this paper.

Figure 3 shows the psda (black line) of the region inside (top) and outside (bottom) the circumpolar ring of cyclones, overlain by the best-fit slopes (red line), for PJ4, PJ6, PJ8, PJ9, PJ11 and PJ13. In every plot, the positions of the Rhines parameter (k_β) and of the transition in slope (k_f) values are also indicated on the wavenumber grid by vertical lines. In addition, we computed the median of the best-fit slopes on all the perijove's passages in order to verify the time variability of the single slopes, and of the k_f points. They are plotted in Figure 3 as black dashed lines above the spectral curves.

As can be seen in Figure 3, the hypothesis of a double power law behavior is confirmed in most cases, except in the PJ8 poleward region and in the PJ13 equatorward region. However, it should be noted that both the slopes, and consequently the position of k_f , depend on the value of the best-fit starting point. This dependence has been noted also by Cosentino et al. (2019) who investigate it by carrying out a sensitivity study on the dependence of the position of the transition in slopes on the k initial value. Future analyses will benefit from their detailed study.

We assigned to all the Rhines parameters the PJ4 value of horizontal velocity, the only one computed so far (Grassi et al., 2018), but this choice is not obvious. Small variations of U have a significant impact on the slope values and on the k_f position. On the other hand, the PJ4 value of horizontal velocity seems adequate in most cases, as confirmed in Table 1, where the best-fit values of the two slopes and the relative medians are reported for all perijoves, together with their 1-σ uncertainty.

Slope values for larger scales, as can be seen in Table 1, are slightly different inside and outside the circumpolar ring, in line with the results obtained in previous works (Harrington et al., 1996; Barrado-Izagirre et al., 2009; Choi & Showman, 2011). Results for smaller scales are more uniform relative to those of slope 1. However, slope 2 values appear somewhat larger than those

reported in the literature cited above. Hypotheses to explain these findings are described in section **5**.

As shown in Table 1, the break in slope k_f exhibits more variability inside than outside the ring. However, the median values are equal in the two cases, with uncertainties that reflect the differing extent of variability. On the other hand, if we refer to the non-dimensional zonal wavenumber k_z, we obtain median values rather different for the poleward (36.6±17.0) and equatorward region (109.7±7.1). These results differ in detail from those reported in Harrington et al. (1996), Barrado-Izagirre et al. (2009) and Choi & Showman (2011), even though they see a large variability in the k_f values.

Figure 3 shows also variability of the integrated power under the curves with time. Although a detailed analysis is beyond the principal aims of our investigation, a simple visual inspection of the plots in Figure 3 shows that contributions from the integrated radiance inside the circumpolar ring varies with time, with the largest integrated power registered during PJ4, while this behavior is not so evident for the integrated psda outside the ring.

4. Wave visualization

Our periodogram analysis reveals some time variability in slope 1 and slope 2 values (Table 1), possibly related to dynamical changes where atmospheric waves may play a role. The high resolution of the images that compose the mosaics of Figure 1, allows for a thorough search for a

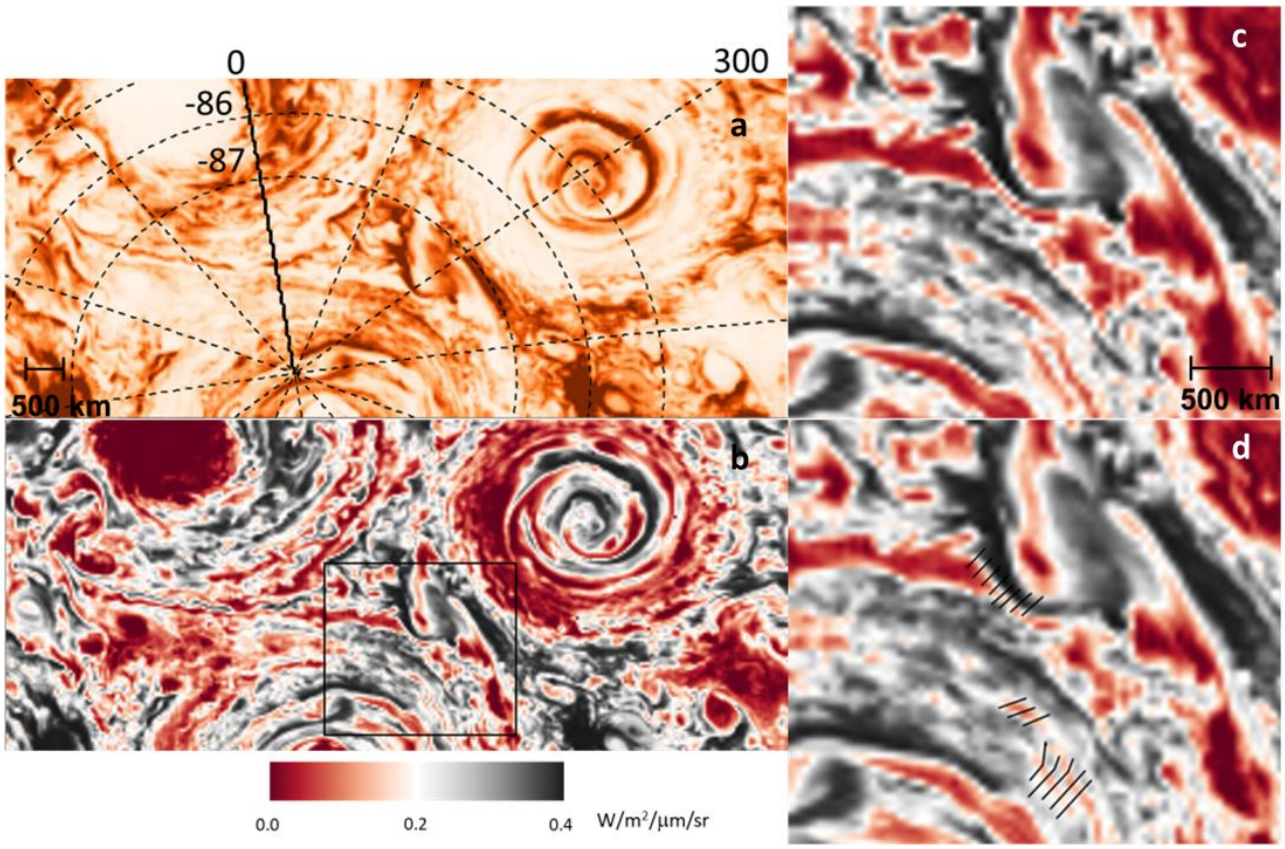

Figure 4- Example of JIRAM image JIR_IMG_RDR_2017033T150327 (~47 km/pixel) acquired during the 4th perijove, and identification of wavy structures. (a) The original JIRAM image where PG latitude and longitude are projected as a reference. (b) Enhanced view of the JIRAM image, highlighting wavy structures. The rectangular region identifies the area where waves are searched. (c) Selected region, extracted from the enhanced view of the image. (d) Selected region with wavy patterns marked with black tickmarks, that identify some crests and troughs visible by eye, and blue arrows pointing to further wavy features. Wavelengths of the marked wave-like features are in the range of 70-100 km. The 500 km horizontal scale is added to panels (a) and (c) for comparison.

possible wave presence in some parts of the southern polar region. We establish a criterion for identifying periodic patterns of banded clouds of at least three alternating crests and troughs to identify a wave.

The JIRAM JIR_IMG_RDR_2017033T150327 image, acquired during the 4th perijove passage of Juno over Jupiter's South Pole, is shown in Figures 4 and 5. We choose this image for its spatial resolution (~ 47 km/pixel), better than the average value (55 km/pixel) of the entire sequence.

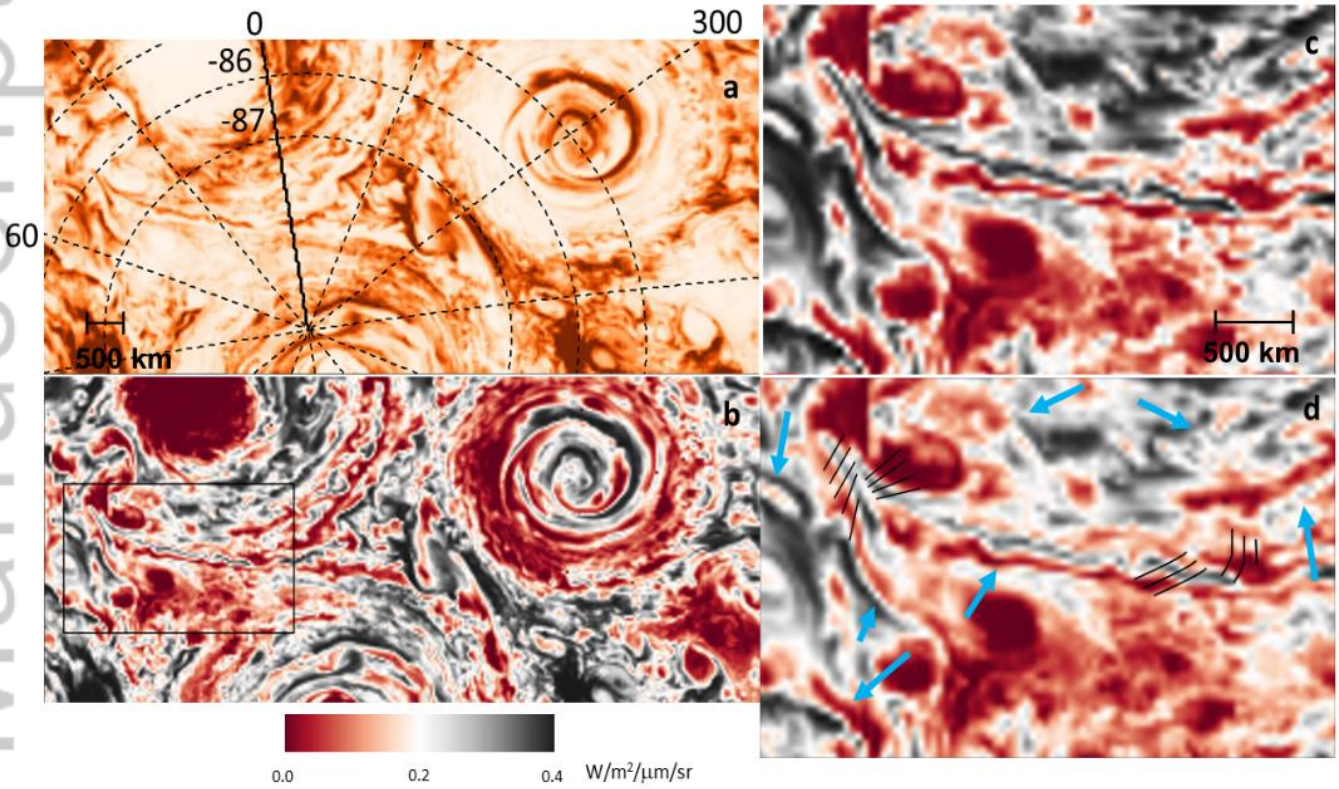

Figure 5 - Same as in Figure 4, applied to a different region. Areas of possible wave interaction (black tickmarks) are visible in panels c and d where two filamentary systems seem to join (upper left corner) and at the end of the right filament.

Many wave-like features are visible when the image is enlarged. Examples of the wavy structures, identified on two rectangular areas in this JIRAM image, are provided in Figures 4 and 5.

We choose to expand areas belonging to the region poleward of the cyclones' ring, one where JIRAM had the most coverage at high resolution. Both Figures 4 and 5 are organized in four panels, where the original pixelation has been interpolated by a bicubic kernel, one of the ENVI tools for enhancing the image visualization. In panel (a) the original image is reported, with the 500 km horizontal scale and the PG geographical grid overlapped. Color scale of this panel is equal to that of Figure 1. Panel (b) shows the same image but with a suitable combination of color stretching - histogram equalization relative to the areas of interest - and color scales applied to enhance the undulating patterns. In this panel, black rectangles identify the zoomed in regions of panels (c) and (d), which represent in turn equal areas without (panel c) and with (panel d) overlaying annotations, employed to highlight some of the wave-like features for ease of

identification. Black ticks are used when crests and troughs are more evident, blue arrows in the other cases.

In Figures 4c and 4d the annotated waves generally seem to propagate zonally, i.e. along lines of equal latitude, but showing different degrees of inclination of the crest directions with respect to the tangent to the latitude circle. This may indicate a greater or lesser proximity of the waves to the main circulation of the cyclones, that could strain the original wave fronts and twist the initial wave direction. A different situation can be seen in Figures 5c and 5d, where the scene is dominated by an area with filamentary structures. In detail, two filamentary systems seem to join in the upper corner of Figures 5c and 5d with waves propagating along both branches of the structure. The most evident crests (black tickmarks) are visible in the area where the two filaments are conjoined, and hence where the two waves might interact. Another area of possible wave interaction is visible at the end of the right filament, where two wave-like features (black tickmarks) seem to cross each other. Several other undulating patterns visible in the zoomed in region have been annotated by blue arrows. It is noteworthy that the directions of propagation of the waves imaged in Figures 5c and 5d seem quite random and not aligned with the latitude circles, in contrast to those in Figures 4c and 4d. As the horizontal wind speed (Grassi et al., 2018) does not change between the two regions, different mechanisms might be acting in the two areas. Waves visualized in Figures 4 and 5 show wavelengths in the range of 70-100 km.

5. Discussion

The results described in section 3 come from the application of well-established methods of data analysis, which were successfully used in the past to describe the spatial structure of Jupiter's cloud patterns at various depths, and their relationship to turbulence (Harrington et al., 1996; Barrado-Izagirre et al., 2009; Choi & Showman, 2011; Cosentino et al., 2017). Because previous studies refer to Jupiter's low and middle-latitudes, a comparison between those findings and ours has little significance, considering the very different dynamical contexts. However, in both cases the power spectra are best fitted by two slopes with similar power laws. All these slopes, including our own values, show some deviations from the values predicted from pure 2D turbulence theory (Kraichnan, 1967; 1971).

The classical 2D and 3D (Kolmogorov, 1941) turbulence equations predict different values for the slopes of the power laws, depending on the turbulent regime. In the 3D turbulent regime there is only one slope, the energy cascade is downscale and the energy is transferred from large to smaller scales, with a $k^{-5/3}$ law. The rigorous 2D theory, governed by the 2D Navier-Stokes equation, introduces the notion of an inverse cascade of energy, or a transfer of energy from small to larger scales beginning at the forcing wavenumber. It is applied to incompressible fluids and predicts two inertial intervals, above and below the forcing scale, namely an inverse energy and a direct enstrophy cascade, where the enstrophy (the integral of the square of the vorticity) accounts for the dissipative effects arising from rotation, vortex formation and generally any swirling activity in the flow. The upscale energy flux should give, according to the theory, a $k^{-5/3}$ power law, while the downscale enstrophy flux should give a power law with slope -3. The median values

calculated from JIRAM data for the upscale slopes were -0.9 (poleward) and -1.2 (equatorward), whereas the equivalent median values for the downscale slopes were -3.2 and -3.4. However, large-scale geophysical flows, although nearly two-dimensional, show deviations from the predictions of strictly 2D fluid dynamics.

A dimensionless parameter relevant to the atmospheric dynamics and turbulence is the Rossby number $Ro=U/fL$, where U is the background wind speed, L is the horizontal scale of the disturbance associated with the phenomenon under study and f is the Coriolis parameter. Ro gives a measure of the significance of rotation apparent forces on the phenomenon under study.

In quasi-geostrophic approximation, the flow is nearly in geostrophic balance but with an inertial contribution significantly smaller than the Coriolis one ($Ro<<1$). Indeed, the quasi-geostrophic equations, in their stream function formulation, differ from the Navier-Stokes ones for the terms depending on Ro^{-1} (Foster et al., 2013). As in the classical 2D turbulence, energy and enstrophy are conserved, but the Coriolis predominance on the inertial term makes vortex stretching possible.

With reference to the transition wavenumbers reported in Table 1, the horizontal length scale $L=1/k_f$, implies for Ro, with $f \cong 3.5 \times 10^{-4}\ s^{-1}$ at polar latitudes, values in the range $\cong 0.08 - 0.1$. These are compatible with the hypothesis of quasi-geostrophic 2D turbulence used in this analysis.

Various dissipation mechanisms can disrupt the steady-state characteristics of the turbulent regime. Friction and wave-wave interaction can determine a transfer of energy and enstrophy in the reciprocal inertial ranges (Maltrud & Vallis, 1993; Young & Read, 2017), modifying the expected slopes. In particular, the physical meaning of nonlinear wave-wave interactions is that resonant sets of wave components exchange energy, redistributing it over the spectrum (Phillips, 1960). In shallow-water models three-wave interactions (so-called triad interactions) become important. Evidence of the influence of nonlinear triad interactions on the transfer of kinetic energy through the whole range of length scale has been reported by Young & Read (2017). They used datasets, acquired in the visible and near-infrared bands in December 2000 during the NASA Cassini mission, to determine the direction of Jupiter's kinetic energy cascade throughout the range of length scales of their specific observations. They found that a transfer of energy occurs not only upscale of the spectral "kink", as expected in quasi-geostrophic two-dimensional turbulence, but also downscale in a non-negligible component. Computing the spectral fluxes of kinetic energy both directly, from two of their datasets, and by calculating nonlinear triad interactions, from the third one, they found that eddy-eddy interactions contribute significantly. Although this computation refers to middle-to-low latitudes, it may be considered valid in whatever region of Jupiter presents similar conditions.

Figures 4 and 5 show that many wave-like features are present on Jupiter's South Pole, concealed by the large-scale cloud patterns, and that some of them might interact, as described in section 4.

A complete overview of the various wave typologies and of the possible implied dynamic scenarios on Jupiter's polar regions is beyond the purpose of this work. Here we note only that several wave-like features propagating in different directions are visible in Figures 4 and 5,

sometimes crossing each other, and thus the conditions for triad interactions are present in the studied region. In the absence of time-resolved images of these waves, we cannot tell whether these are diverging or converging, but the structure is suggestive of the triad interactions discussed above. If this is the case, it provides one possible hypothesis to explain the deviation of the slopes from the theoretical 2D power laws. A full in-depth analysis using the 2D filtering method will be published in a paper in preparation. The waves highlighted in Figures 4 and 5 are not the only ones present in these figures, but they were selected to serve as clear illustrations of the plethora of such waves we see in the best JIRAM images of the southern polar region.

The k_f transition in slope, obtained in this work, indicates that a forcing scale can exist around 500 km. If we hypothesize that baroclinic instabilities play a non-negligible role in the region under investigation, then we can assign to L the L_d Rossby deformation radius meaning (Pedlosky, 1986). It must be noted that the L_d values, reported in the Jovian literature, have been quite different so far, with values O(10^3 km) (Harrington et al., 1996**;** Young & Read, 2017). However, those values have been estimated for different pressure levels and at different latitudes. We use the same approach as Conrath et al. (1981), that refers to data acquired during Voyagers missions of the Jovian stratosphere, but using values of the various parameters derived from the Galileo mission, adjusted to a tropospheric depth down to $p_0 \cong 5$ bar.

Specifically, the deformation radius is

$$L_d = \frac{H}{f} \times N$$

where H is the vertical scale height, f the Coriolis parameter and N the Brunt–Väisälä (buoyancy term) frequency. H is computed from $H = RT/g \cong 23$ km, with T≅ 180 K, calculated as the mean between $p_2 = 0.03$ bar (low stratosphere) and $p_1 = 5$ bar (deepest sounding level of JIRAM) pressure levels, the gas constant R=3600 J kg^{-1} K^{-1}) and the gravity acceleration g=28.3 m s^{-2}, at polar latitudes.

The Brunt–Väisälä frequency for the troposphere assumes values ranging in the interval 0.01-0.006 s^{-1} (Watkins & Cho, 2013; Magalhães et al., 2002). Accordingly, the Rossby deformation radius values vary from L_d ~ 650 km to L_d ~ 395 km, in agreement with the median value of $1/k_f$ (Table 1).

These values of L_d at Jupiter's South Pole, converted into the planetary Burger number $Bu = \left(\frac{L_d}{R_c}\right)^2$, with R_c being the polar radius of curvature, yield Bu~0.3-0.7× 10^{-4}. The planetary Burger number is a dimensionless parameter indicating the importance of the fluid stratification on the dynamics. Our findings agree with the polar dynamical regime which Brushaber et al. (2019) define as "Jupiter-like". In this regime Bu~10^{-4} , while values typical for Saturn and ice giant polar dynamics are Bu~10^{-3} and Bu~10^{-2}, respectively. "Jupiter-like", "Saturn like" and "Uranus/Neptune like" polar regimes are characterized in order by multiple circumpolar cyclones, a compact intense cyclonic polar vortex and a large cyclonic polar vortex.

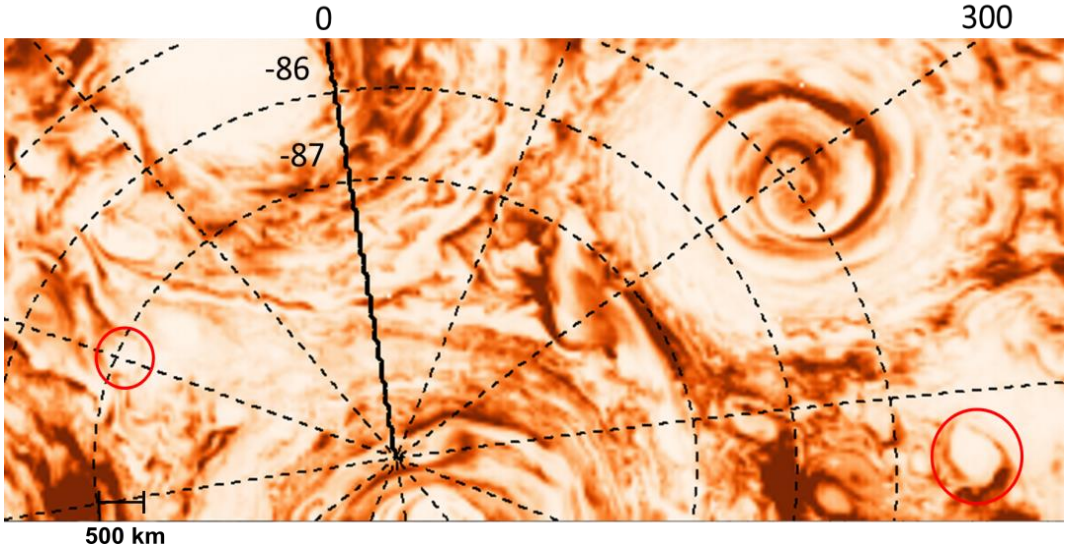

Figure 6 - Comparison of the 500 km scale and eddies located close to the region poleward the cyclone's ring, as seen in the JIRAM image JIR_IMG_RDR_2017033T150327.

On the other hand, L_d can be thought of as the horizontal scale at which rotation effects become as important as buoyancy effects. Thus, if we interpret $1/k_f$ as the Rossby deformation radius, we expect there should be some eddies and/or meanders in the flow with the same horizontal scale of L_d in the regions under study. In Figure 6 the 500 km horizontal scale is compared with a couple of small eddies (red circle) at the limit of the poleward region.

Consequently, the comparison between the power spectrum analysis and the dynamical structures in Figures 4, 5 and 6 suggests the presence of some baroclinic instabilities in the region sampled in this study. We speculate that this finding is compatible with a two-layer model, with horizontal gradients of temperature parallel to isobaric contours deep in the atmosphere (equivalent barotropic atmosphere) and a thin upper layer where temperature gradients cross the isobars and baroclinic instabilities transfer energies from ~ 500 km toward larger scales. This can be a possible scenario if the deep atmosphere, embedded between the central cyclone and the circumpolar ring, does not experience any mixing with warm air masses associated with the cyclonic circulations. Recently, Aurnou et al. (2018) suggested in their gas giant convection model a similar scenario, characterized by a thick stable layer with strong stability, and deep polar cyclones, perhaps penetrating to ~ 3000 km, i.e. the depth of the zonal jets, or even deeper according to Reinaud (2019). The low variability of the slopes in Table 1 throughout the various perijoves suggests that this scenario persists for at least months or years.

6. Conclusions

We used a power spectrum analysis on Jupiter's polar cloud opacities to infer what type of turbulent regime is acting on the regions just outside and inside the cluster of cyclones encircling the South Pole. We found that the shape of the power spectra is compatible with a quasi-

geostrophic two-dimensional turbulent regime, both for the equatorward and poleward annular regions considered here, with forcing scale around 500 km. We also found that this regime is preserved, with few variations, in six out of ten Juno orbits around Jupiter, spanning an overall period of roughly 1.5 years. The slight difference between the slopes in this work and the theoretical $k^{-5/3}$ and k^{-3} power laws can have more than one reason. The presence of minor vortices along some brightness circular paths or dissipation mechanisms, like the triad interaction, that redistribute energy and enstrophy on different scale ranges are two possible explanations of the deviation from theoretical slopes. A possible hint of the triad interaction is the complex pattern of waves, visible in the JIRAM images after a proper stretching and color scale application. In this work we assumed that the forcing scale can be interpreted as the Rossby deformation radius, a hypothesis that would seem to be confirmed by the presence of eddies and meanders of similar size inside the flow. Finally, we deduce that baroclinic instabilities perturb the region under analysis. This conclusion prompts us to speculate on a possible scenario of deep equivalent-barotropic atmosphere. Additional insights into the puzzling deep dynamics of Jupiter's polar atmosphere will come from the findings of Juno/MWR (MicroWave Radiometer), which senses deeper levels of Jupiter's atmosphere than does JIRAM.

Acknowledgments and Data Statement

We thank F. Bignami from Institute of Marine Sciences (CNR-Italy), A. Provenzale from Institute of Geosciences and Earth Resources (CNR-Italy), J. von Hardenberg from Institute of Atmospheric Sciences and Climate (CNR-Italy) and A. Bracco from the Georgia Institute of Technology (USA) for their comments and helpful discussions. This work was supported by the Italian Space Agency through ASI-INAF contract I/010/10/0 and 2014-050-R.0. Part of this research was also supported by the National Aeronautics and Space Administration, a portion of which funding was provided to the Jet Propulsion Laboratory, California Institute of Technology.

Original JIRAM data used for this work are available at the NASA Planetary Data System website

https://pds-atmospheres.nmsu.edu/data_and_services/atmospheres_data/JUNO/jiram.html.

Maps in Figure 1 and Figure 4 were produced by using the commercial software ENVI (https://www.harrisgeospatial.com/Software-Technology).

The datasets generated during the current study are available at DOI: 10.17632/4f3mrkcxvb.5.

Captions

Figure 1 - Stereographic projections of mosaics composed with images of Jupiter's South Pole acquired by IMG-M in six Juno perijoves. All the images have been corrected for the emission angle and re-scaled in the same range of radiance values. Here, aerosol-free regions of high radiance are dark, and aerosol-covered regions of low radiance are white, as reported in the color

bar at the bottom of the figure. Black solid circles indicate the trajectories along which the analyzed signals have been sampled. The 80° S planetographic latitude is reported as reference (black dotted circle) in each mosaic.

Figure 2 - Average of three power spectral densities relative to the signals sampled outside the southern circumpolar ring of cyclones during PJ4. The error bars represent the standard error of the mean.

Figure 3 - Averages of power spectra of the signals sampled inside (top) and outside (bottom) the southern circumpolar ring of cyclones. Power law fits overlap the spectra (red line). Median values of the overall power laws for the two cases are shown above the spectra (dashed black lines). The positions of the wavenumbers corresponding to the Rhines scale and to the transition in slope are marked by vertical lines. X axes at bottom of each plot are in wavenumbers – inverse of length – while x axes at the top are in zonal wavenumbers, as defined in the text.

Figure 4 - Example of JIRAM image JIR_IMG_RDR_2017033T150327, (~47 km/pixel) acquired during the 4th perijove, and identification of wavy structures. (a) The original JIRAM image where PG latitude and longitude are projected as a reference. (b) Enhanced view of the JIRAM image, highlighting wavy structures. The rectangular region identifies the area where waves are searched. (c) Selected region, extracted from the enhanced view of the image. (d) Selected region with wavy patterns marked with black tickmarks, that identify some crests and troughs visible by eye, and blue arrows pointing to further wavy features. Wavelengths of the marked wave-like features are in the range of 70-100 km. The 500 km horizontal scale is added to panels a and c for comparison.

Figure 5 - Same as in Figure 4, applied to a different region. Areas of possible wave interaction (black tickmarks) are visible in panels c and d where two filamentary systems seem to join (upper left corner) and at the end of the right filament.

Figure 6 - Comparison of the 500 km scale and eddies located close to the region poleward the cyclone's ring, as seen in the JIRAM image JIR_IMG_RDR_2017033T150327.

Table 1 – Best-fit slope values for the psda of the datasets relative to different perijoves. "Poleward" and "Equatorward" table sections correspond to psda computed by signals sampled inside and outside the circumpolar ring of cyclones. We report the values of the two slopes, the 1-σ uncertainty value for each slope fit and the wavenumber value in correspondence of the transition in slope. At the bottom of each column of the table the medians are shown.

References

Acton, C. H. (1996). *Ancillary data services of NASA's Navigation and Ancillary Information Facility*. Planetary and Space Science, 44(1), 65–70. https://doi.org/10.1016/0032-0633(95)00107-7

Adriani, A. et al. (2019). *Two-Years Observations of the Jupiter Polar Regions by JIRAM on board Juno*". Submitted to Journal of Geophysical Research: Planets.

Adriani, A., Filacchione, G., di Iorio, T., Turrini, D., Noschese, R., Cicchetti, A., et al. (2014). *JIRAM, the Jovian infrared auroral mapper*. Space Science Reviews, 213(1-4), 393–446. https://doi.org/10.1007/s11214-014-0094-y.

Adriani, A., Mura, A., Orton, G. S., Hansen, C., Altieri, F., Moriconi, M. L., et al. (2018). *Clusters of cyclones encircling Jupiter's poles*. Nature, 555(7695), 216–219. https://doi.org/10.1038/nature25491.

Aurnou, J. M., Heimpel, M. H., & Featherstone, N. A. (2018). *Simulating Atmospheric Features of Jupiter and Saturn With Deep Convection Models*. Paper presented at Fall Meeting 2018, American Geophysical Union, New Orleans, Louisiana.

Barrado-Izagirre, N., Pérez-Hoyos, S., & Sánchez-Lavega, A. (2009). *Brightness power spectral distribution and waves in Jupiter's upper cloud and hazes*. Icarus, 202(1), 181-196. doi:10.1016/j.icarus.2009.02.015.

Bendat, J. S., & Piersol, A. G. (1986). *Random Data: Analysis and Measurement Procedures*. New York: Wiley, 566 pp.

Bevington, P. H., & Robinson, D. K. (1992). *Data Reduction and Error Analysis for the Physical Sciences.* McGraw.Hill (2nd ed.), 328 pp.

Brueshaber, S. R., Sayanagi, K. M., & Dowling, T. E. (2019). *Dynamical regimes of giant planet polar vortices.* Icarus, 323, 46-61. doi: 10.1016/j.icarus.2019.02.001.

Choi, D. S., & Showman, A. P. (2011). *Power spectral analysis of Jupiter's clouds and kinetic energy from Cassini.* Icarus, 216(2), 597-609. doi:10.1016/j.icarus.2011.10.001.

Conrath, B. J., Gierasch, P. J., & Nath, N. (1981). *Stability of Zonal Flows on Jupiter*. Icarus, 48, 256-282.

Cosentino, R. G., Butler, B., Sault, B., Morales-Juberías, R., Simon, A., de Pater, I. (2017). *Atmospheric waves and dynamics beneath Jupiter's clouds from radio wavelength observations*. Icarus, 292, 168-181. doi: 0.1016/j.icarus.2017.01.006.

Cosentino, R. G., Simon, A., & Morales-Juberías (2019). *Jupiter's Turbulent Power Spectra From Hubble Space Telescope*. Journal of Geophysical Research: Planets, 124, 1204–1225. https://doi.org/10.1029/2018JE005762

Danilov, S. D., & Gurarie D. (2000). *Quasi-two-dimensional turbulence*. Uspekhi Fizicheskikh Nauk, 170 (9), 921 – 968. doi: 10.1070/PU2000v043n09ABEH000782.

Foster, E. L., Iliescu, T., & Wang, Z. (2013). *A Finite element discretization of the streamfunction formulation of the stationary quasi-geostrophic equations of the ocean.* Comput. Methods Appl. Mech. Engrg. 261–262, 105-117, https://doi.org/10.1016/j.cma.2013.04.008.

565 Grassi, D., Adriani, A., Mura, A., Dinelli, B. M., Sindoni, G., Turrini, D., et al. (2017).
566 *Preliminary results on the composition of Jupiter's troposphere in hot spot regions from the*
567 *JIRAM/Juno instrument*. Geophysical Research Letters, 44, 4615–4624. doi:
568 10.1002/2017GL072841.

569 Grassi, D., Adriani, A., Moriconi, M. L., Mura, A., Tabataba-Vakili, F., Ingersoll A. P., et al.
570 (2018). *First Estimate of Wind Fields in the Jupiter Polar Regions From JIRAM-Juno Images*.
571 Journal of Geophysical Research: Planets, 123(6), 1511-1524. doi:10.1029/2018JE005555.

572 Harrington, J., Dowling, T.E., & Baron, R. L. (1996). *Jupiter's Tropospheric Thermal Emission*
573 *II: Power Spectrum Analysis and Wave Search*. Icarus, 124, 32–44.
574 https://doi.org/10.1006/icar.1996.0188.

575 Ingersoll, A. P., Dowling, T. E., Gierasch, P. J., Orton, G. S., Read, P. L., Sánchez-Lavega, A., et
576 al. (2004). *Dynamics of Jupiter's Atmosphere*. in Jupiter: The planet, satellites and magnetosphere,
577 Cambridge University Press, 719 pp.

578 Irwin, P. G. J., Weir, A. L., Taylor, F. W., Calcutt, S. B., Carlson, R. W. (2001). *The Origin of*
579 *Belt/Zone Contrasts in the Atmosphere of Jupiter and Their Correlation with 5 μm Opacity*.
580 Icarus, 149(2), 397-415. doi:10.1006/icar.2000.6542.

581 Kolmogorov, A. N. (1941). *The local structure of turbulence in incompressible viscous fluid for*
582 *very large Reynolds numbers*. Doklady Akademiia Nauk SSSR, 30, 301-305.
583 https://www.jstor.org/stable/51980.

584 Kraichnan, R. H. (1967). *Inertial Ranges in Two-Dimensional Turbulence*. Physics of Fluids, 10,
585 1417-1422. https://doi.org/10.1063/1.1762301.

586 Kraichnan, R. H. (1971). *Inertial-range transfer in two- and three-dimensional turbulence*.
587 Journal of Fluid Mechanics, 47, 525-535. https://doi.org/10.1017/S0022112071001216.

588 Kunde, V., Hanel, R., Maguire, W., Gautier, D., Baluteau, J. P., Marten, A., et al. (1982). *The*
589 *tropospheric gas composition of Jupiter's north equatorial belt (NH_3, PH_3, CH_3D,GeH_4, H_2O) and*
590 *the jovian D/H isotopic ratio*. Astrophysical Journal, 263, 443–467. doi:10.1086/160516.

591 Magalhães, J. A., Seiff, A., & Young, R. E. (2002). *The Stratification of Jupiter's Troposphere at*
592 *the Galileo Probe Entry Site*. Icarus, 158(2), 410-433. doi:10.1006/icar.2002.6891.

593 Maltrud, M. E., & Vallis, G. K. (1993). *Energy and enstrophy transfer in numerical simulations of*
594 *two-dimensional turbulence*. Physics of Fluids A: Fluid Dynamics, 5(7), 1760-1775. doi:
595 10.1063/1.858851.

596 Orton, G. S., Hansen, C., Caplinger, M., Ravine, M., Atreya, S., Ingersoll, A. P., et al. (2017). *The*
597 *first close-up images of Jupiter's polar regions: Results from the Juno mission JunoCam*
598 *instrument*. Geophysical Research Letters, 44, 4599–4606.
599 https://doi.org/10.1002/2016GL072443.

600 Pedlosky, J. (1986). *Geophysical Fluid Dynamics*, Springer (2nd ed.), 710 pp.

Peralta, J., Hueso, R., & Sánchez-Lavega, A. (2007). *Cloud brightness distribution and turbulence in Venus using Galileo violet images.* Icarus, 188(2), 305-314. doi:10.1016/j.icarus.2006.12.005.

Phillips, O. M. (1960). *On the dynamics of unsteady gravity waves of finite amplitude*. Journal of Fluid Mechanics, 9(2), 193-217. doi:10.1017/S0022112060001043.

Reinaud, J. N. (2019). *Three-dimensional quasi-geostrophic vortex equilibria with m-fold symmetry*. Journal of Fluid Mechanics, 863, 32-59. doi:10.1017/jfm.2018.989.

Rhines, P. B. (1975). *Waves and turbulence on a beta-plane*. Journal of Fluid Mechanics, 69(3), 417-443. https://doi.org/10.1017/S0022112075001504.

Sada, P. V., Beebe, R. F., & Conrath, B. J. (1996). *Comparison of the Structure and Dynamics of Jupiter's Great Red Spot between the Voyager 1 and 2 Encounters*. Icarus, 119(2), 311-335. doi: 10.1006/icar.1996.0022.

Sánchez-Lavega, A., & Heimpel, M. (2018). *Atmospheric Dynamics of Giants and Icy Planets*. in Handbook of Exoplanets, H.J. Deeg, J.A. Belmonte (eds.), 3490 pp. doi: 10.1007/978-3-319-30648-3_51-1.

Travis, L. D. (1978). *Nature of the Atmospheric Dynamics on Venus from Power Spectrum Analysis of Mariner 10 Images.* Journal of the Atmospheric Sciences, 35, 1584-1595. https://doi.org/10.1175/1520-0469(1978)035<1584:NOTADO>2.0.CO;2

Watkins, C., & Cho, J. Y-K. (2013). *The vertical structure of Jupiter's equatorial zonal wind above the cloud deck, derived using mesoscale gravity waves*. Geophysical Research Letters, 40(3), 472-476, doi:10.1029/2012GL054368.

Young, R. M. B., & Read, P. L. (2017). *Forward and inverse kinetic energy cascades in Jupiter's turbulent weather layer.* Nature Physics,13, 1135-1142. doi: 10.1038/NPHYS4227.

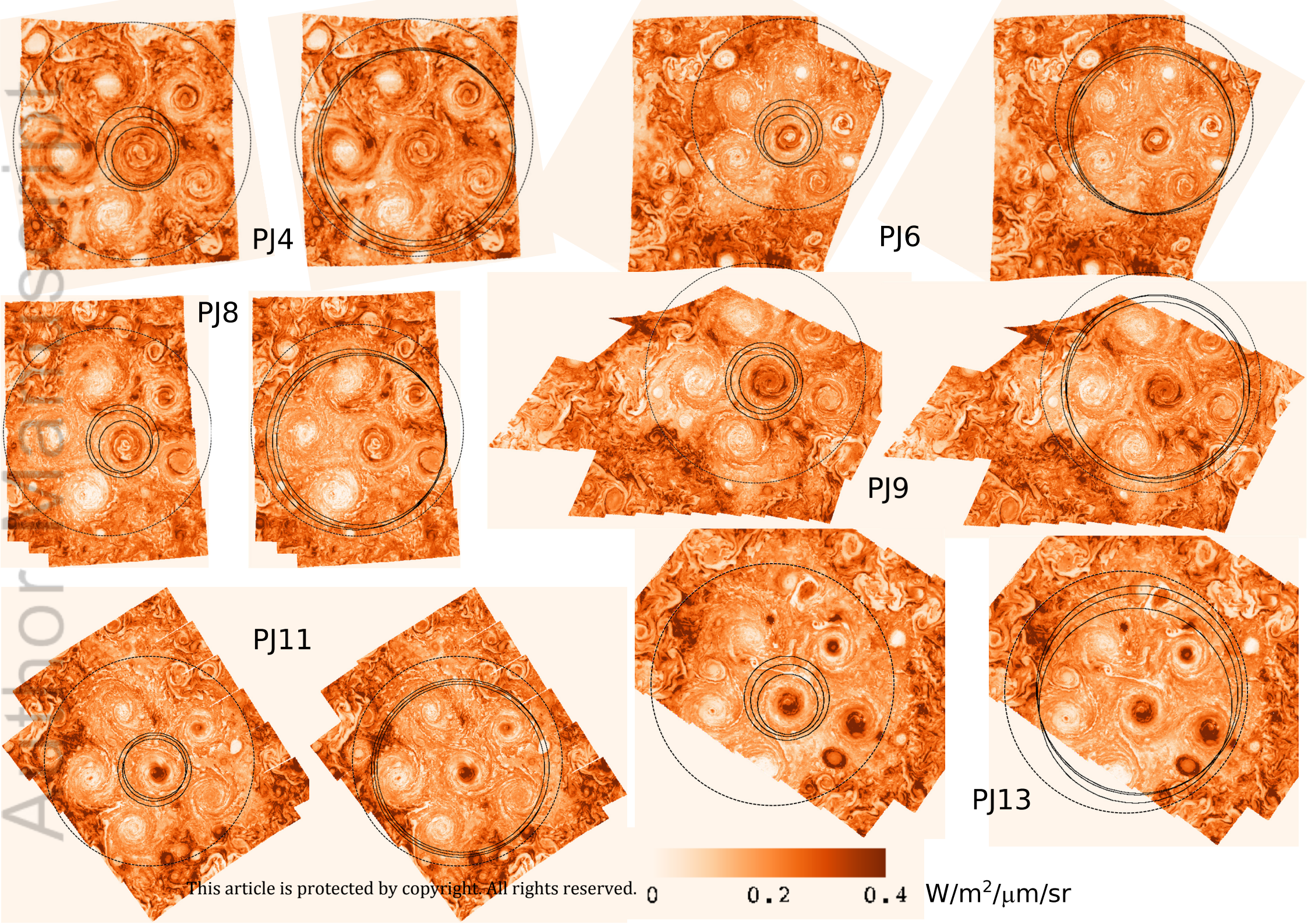

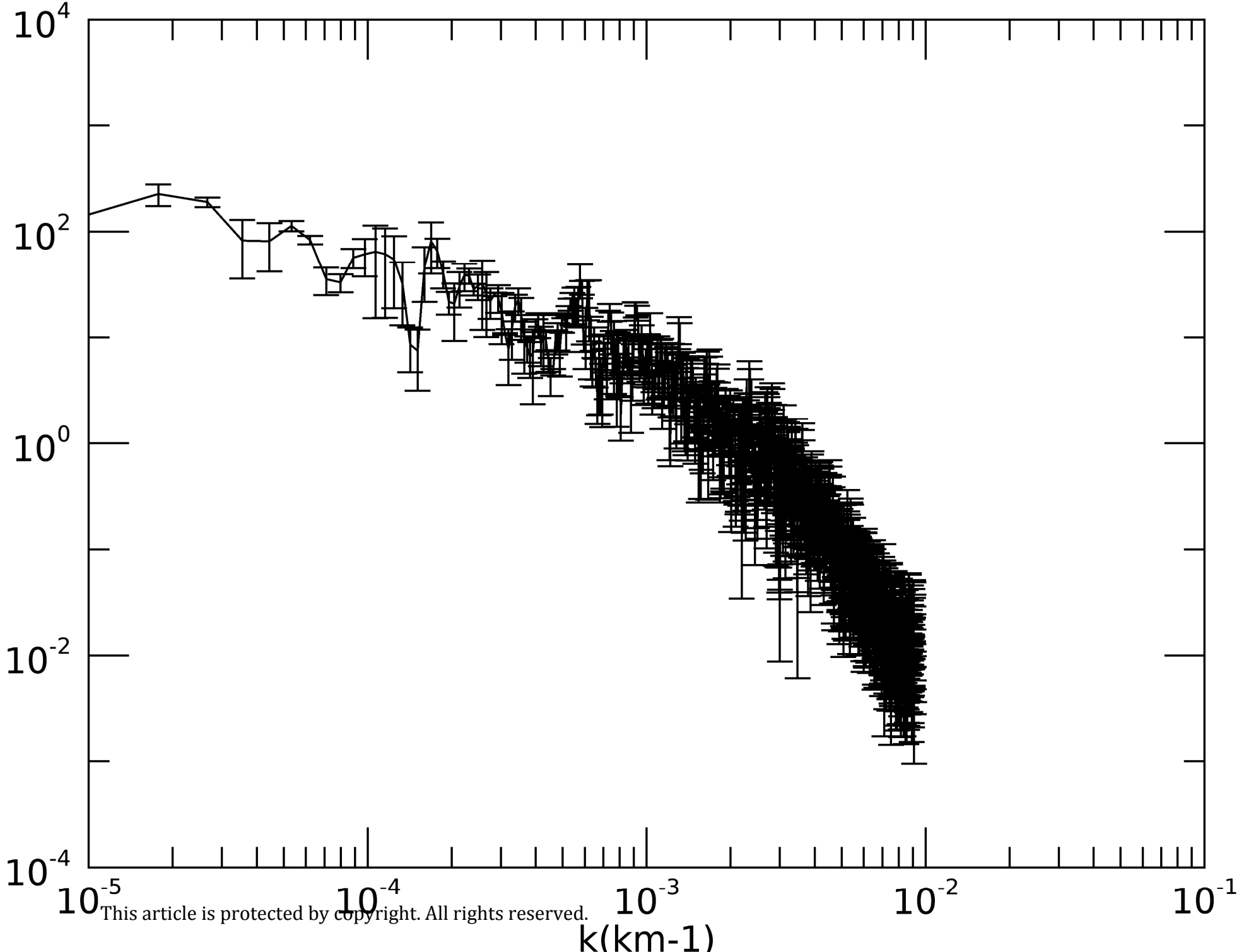

Poleward

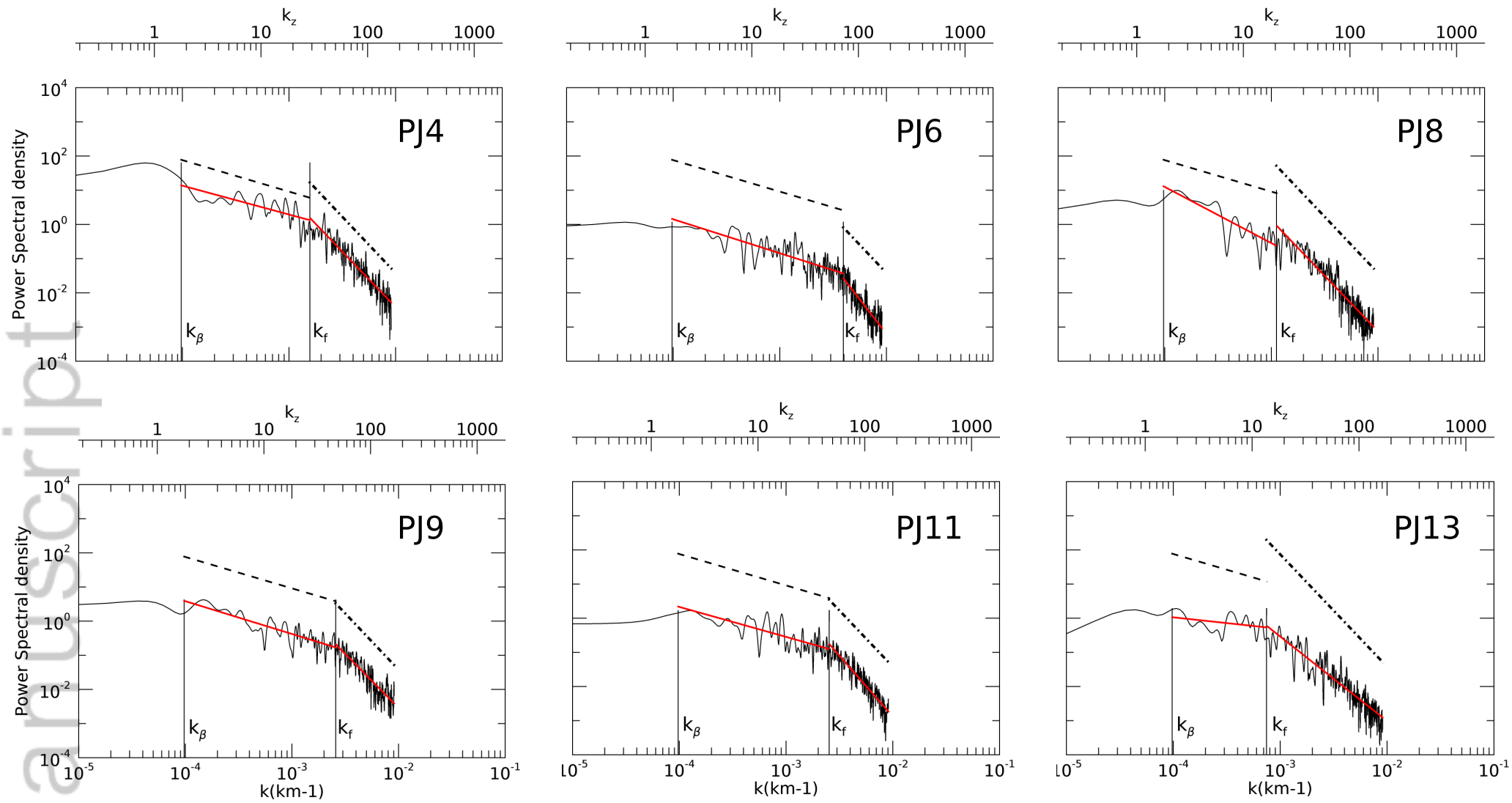

Equatorward